JACS
JOURNAL OF THE AMERICAN CHEMICAL SOCIETY
pubs.acs.org/JACS
Article

Dipole Engineering through the Orientation of Interface Molecules for Efficient InP Quantum Dot Light-Emitting Diodes

Seungjin Lee,[#] So Min Park,[#] Eui Dae Jung,[#] Tong Zhu,[#] Joao M. Pina, Husna Anwar, Feng-Yi Wu, Guan-Lin Chen, Yitong Dong, Teng Cui, Mingyang Wei, Koen Bertens, Ya-Kun Wang, Bin Chen, Tobin Filleter, Sung-Fu Hung, Yu-Ho Won, Kwang Hee Kim, Sjoerd Hoogland, and Edward H. Sargent*

Cite This: https://doi.org/10.1021/jacs.2c09705

Read Online

ACCESS | Metrics & More | Article Recommendations | Supporting Information

ABSTRACT: InP-based quantum dot (QD) light-emitting diodes (QLEDs) provide a heavy-metal-free route to size-tuned LEDs having high efficiency. The stability of QLEDs may be enhanced by replacing organic hole-injection layers (HILs) with inorganic layers. However, inorganic HILs reported to date suffer from inefficient hole injection, the result of their shallow work functions. Here, we investigate the tuning of the work function of nickel oxide (NiO_x) HILs using self-assembled molecules (SAMs). Density functional theory simulations and near-edge X-ray absorption fine structure put a particular focus onto the molecular orientation of the SAMs in tuning the work function of the NiO_x HIL. We find that orientation plays an even stronger role than does the underlying molecular dipole itself: SAMs having the strongest electron-withdrawing nitro group (NO_2), despite having a high intrinsic dipole, show limited work function tuning, something we assign to their orientation parallel to the NiO_x surface. We further find that the NO_2 group—which delocalizes electrons over the molecule by resonance—induces a deep lowest unoccupied molecular orbital level that accepts electrons from QDs, producing luminescence quenching. In contrast, SAMs containing a trifluoromethyl group exhibit an angled orientation relative to the NiO_x surface, better activating hole injection into the active layer without inducing luminescence quenching. We report an external quantum efficiency (EQE) of 18.8%—the highest EQE among inorganic HIL-based QLEDs (including Cd-based QDs)—in InP QLEDs employing inorganic HILs.

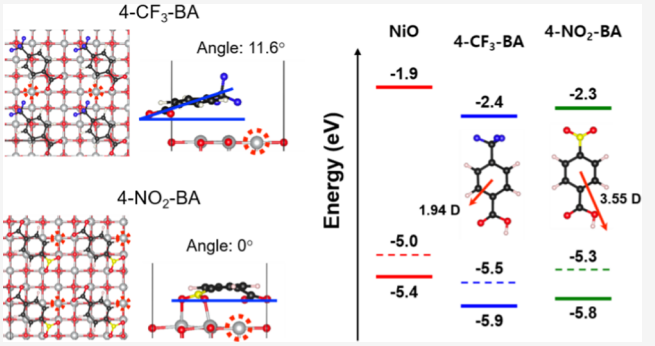

INTRODUCTION

Colloidal quantum dots (QDs) have attracted significant attention for next-generation displays owing to their color tuning, high color purity, and solution processing.[1−3] While InP-based QDs have been used commercially as phosphors in liquid crystal displays, QD-based light-emitting diodes (QLEDs) suffer from limited operating stability for commercial electroluminescent displays.[4−9]

InP QLEDs adopt a p-i-n structure in which the QD-emitting layer is sandwiched between an organic hole injection/transport bi-layer (HIL/HTL) and an inorganic electron transport layer. Poly(3,4-ethylenedioxythiophene):polystyrene sulfonate (PEDOT:PSS) is widely used as the HIL: it provides a smooth surface for the ensuing layers and has a work function that favors hole injection from the indium tin oxide (ITO) anode to the HTL.[1,10,11]

It is the acidic and hygroscopic nature of PEDOT:PSS that leads to etching of the ITO and HTL layers in the presence of moisture and at elevated temperatures, accounting for limited operating stability.[12−15]

NiO_x has the advantage of high hole mobility and materials stability, making it a potentially attractive HIL candidate in QLEDs. Solution-processed NiO_x films have been modified to increase performance and operating stability in CdSe QLEDs.[16,17] However, the work function of NiO_x is 5.0 eV, which is not sufficiently deep to form a low-resistance contact with the organic HTL to achieve efficient hole injection. Solution-processed NiO_x films contain surface defects such as oxygen vacancies that produce luminescence quenching.[18−20]

Self-assembled molecules (SAMs) offer a route to modulate the energy levels of NiO_x and passivate surface defects, improving hole injection and reducing luminescence quenching.[16,21] The energy level shift is a consequence of the net dipole moment induced by SAMs at the interface.[19,22] This net

Received: September 11, 2022

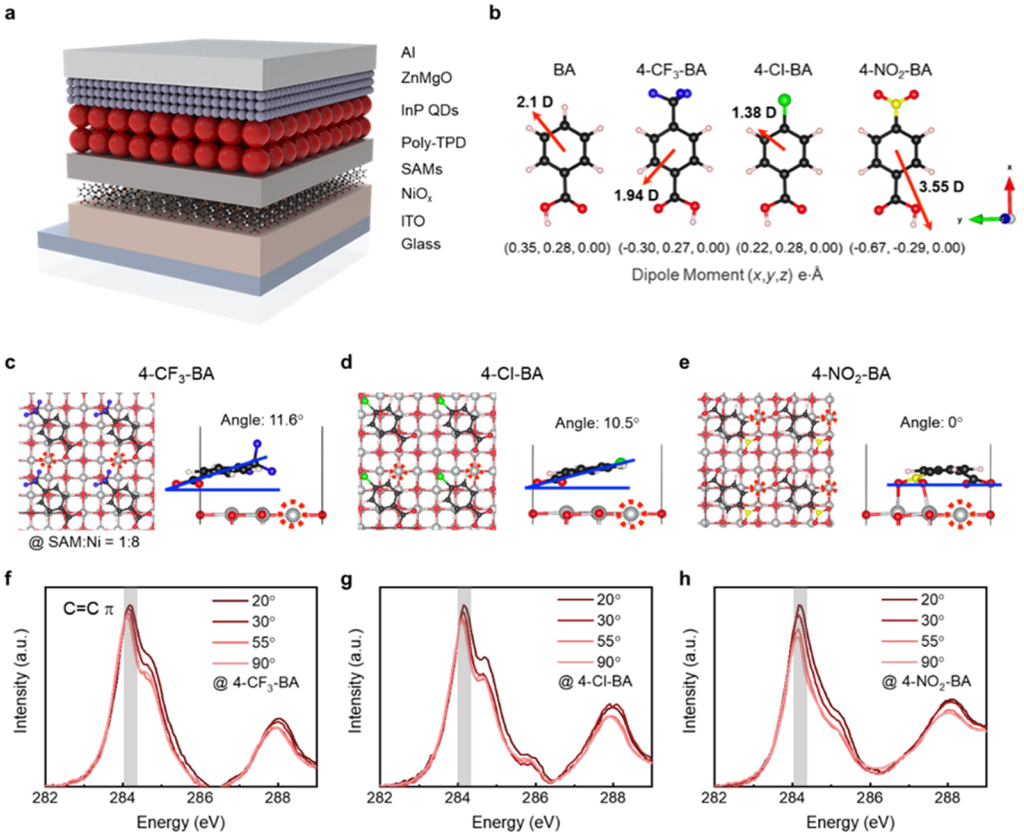

Figure 1. Device, chemical structures, and molecular orientation. (a) Device structure of QLEDs. (b) Molecule dipole moment for BA, 4-CF_3-BA, 4-Cl-BA, and 4-NO_2-BA. Dipole moments are shown in bottom brackets in the (*x*,*y*,*z*) format (in e. Å). Directions are shown in the red arrow within the total value (in Debye) labeled. (c–e) Interfacial structures of SAMs on a NiO_x (001) surface within V_O defect relaxed by DFT. (f–h) NEXAFS spectra of SAMs on NiO_x at various incident angles from 20 to 90°, the angular dependence of benzene π^*-resonance features is highlighted.

dipole arises from the projection of the dipole between the SAM molecule and the NiO_x onto the normal to the NiO_x surface. Prior studies have focused on the selection of tail groups to tune the molecular dipole moment.[19,22,23] Here, an electron-withdrawing tail group would enhance the intrinsic dipole, which would lead to a deepening of the work function. We posited that pointing the SAM molecules in the most favorable (ideally, perpendicular-to-the-surface, a.k.a. the normal direction) orientation required further attention.

We investigate the influence of the tail group on both the intrinsic dipole and also on the molecular orientation, finding that a tail group having a strong electron-withdrawing nature does not guarantee a deep work function for NiO_x. SAMs with a stronger electron-withdrawing nitro (NO_2) group induce a shallower work function than do those containing a trifluoromethyl group (CF_3). This we attribute to the less favorable molecular orientation driven by the binding affinity of the tail group with NiO_x surfaces. We further study the effect of frontier orbitals of SAMs on luminescence quenching and find that the NO_2 group—which could delocalize π-electrons of an aromatic ring by resonance—induces a deep lowest unoccupied molecular orbital (LUMO) level that could accept electrons from QDs, resulting in luminescence quenching. This model was used to achieve an external quantum efficiency (EQE) of 18.8% in InP QLEDs, a record efficiency for QLEDs based on inorganic HILs.

RESULTS AND DISCUSSION

Molecular Orientation and Dipole Moments. QLEDs use a p-i-n structure ITO/PEDOT:PSS/organic HTL/QDs/ZnMgO/Al. We explored replacing PEDOT:PSS with SAM-modified NiO_x (Figure 1a). We choose benzoic acid (BA) derivatives to modify NiO_x because the carboxyl group is expected to anchor to the NiO_x surface. Seeking to combine a strongly electron-withdrawing tail group with a highly polarizable aromatic ring, we introduced NO_2 as the tail group, i.e., 4-nitro BA (4-NO_2-BA) (Figure 1b). To compare the effect of the different tail groups (Figure 1b), we used 4-trifluoromethyl BA (4-CF_3-BA) and 4-chloro BA (4-Cl-BA). 4-NO_2-BA has the strongest computed dipole moment (calculated through standard HSE06[24,25] using density functional theory (DFT)) among molecules investigated, the results of its employment of the strongest electron-withdrawing group, NO_2.

Molecular orientation of SAMs depends on various factors: the chemical structure, including the head group, spacer group, and tail group, packing density, and surface characteristics of substrates.[26,27] A strong affinity of the tail group or space group for the substrate results in a preferential orientation parallel to the surface.[28,29] We then explored, also using DFT, molecular orientation as a function of the tail group (Figure 1c–e) (details of SAM coverage and binding energies between the anchoring group and NiO_x in Figure S1). The tail group of SAMs has a negligible effect on the binding energy between the anchoring group and NiO_x. We further carried out X-ray

https://doi.org/10.1021/jacs.2c09705
J. Am. Chem. Soc. XXXX, XXX, XXX−XXX

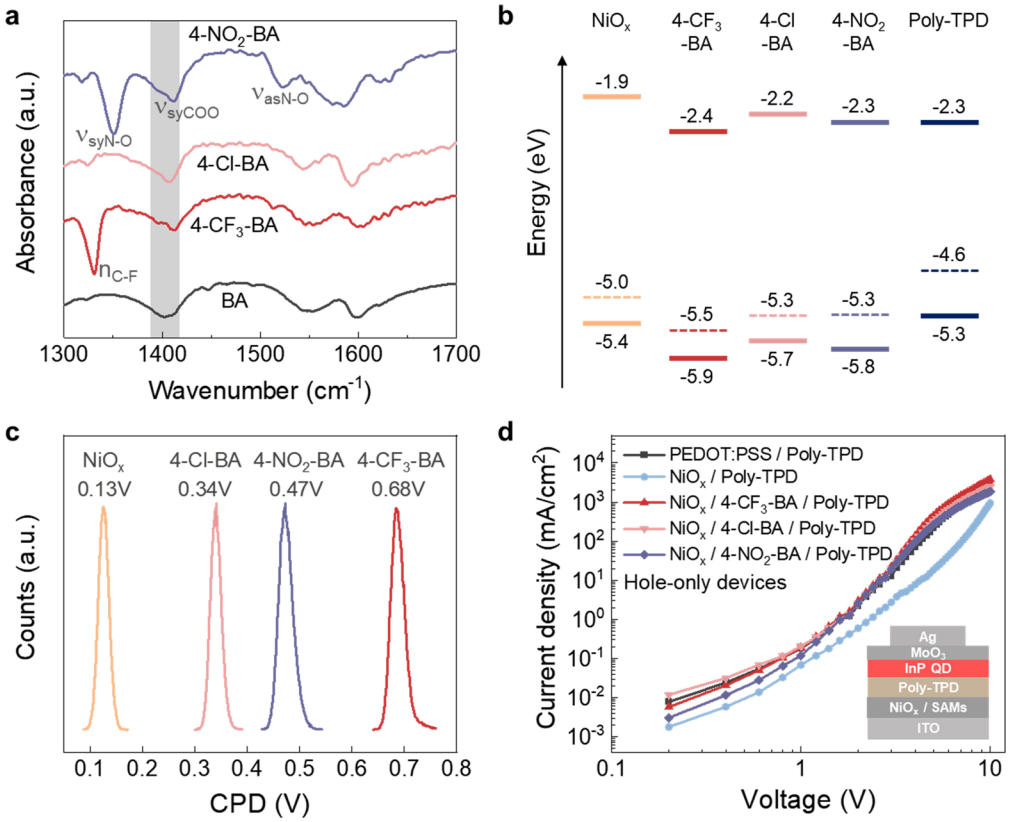

Figure 2. Characterization of energy levels and hole injection. (a) FTIR spectra of SAM-treated NiO_x films. (b) UPS spectra of pristine NiO_x and SAM-treated NiO_x films. (c) SKPM histogram of pristine NiO_x and SAM-treated NiO_x films showing the variation of CPD over the 2 μm × 2 μm area. (d) Current density versus voltage (J–V) characteristics of hole-only devices.

photoelectron spectroscopy (XPS) to investigate the coverage of SAMs on the NiO_x surface (Table S1). The XPS results revealed that the ratio of SAM to Ni atom is 1:17, 1:17, and 1:18 for the NiO_x films with 4-CF_3-BA, 4-Cl-BA, and 4-NO_2-BA, respectively. We did not observe a noticeable difference in SAM coverage on the surface depending on the tail group of SAMs. With DFT we predict angles between SAM and NiO_x (001) of 12, 11, and 0° for 4-CF_3-BA, 4-Cl-BA, and 4-NO_2-BA on NiO_x. The parallel molecular orientation of 4-NO_2-BA is driven by the high binding affinity of the tail group with the NiO_x surface. 4-NO_2-BA has the largest molecular dipole moment (Figure 1b) but its parallel orientation curtails its impact on work function.

In order to estimate experimentally the molecular orientation of SAMs, we performed near-edge X-ray absorption fine structure (NEXAFS) spectroscopy. The corresponding carbon K-edge NEXAFS spectra of SAM-treated NiO_x films were obtained for different photon incidence angles θ between 20 and 90° (Figure 1f–h). The benzene π^*-resonance reports the component of the transition dipole moment perpendicular to the molecular plane of the benzene ring. The 4-NO_2-BA-treated NiO_x films exhibited a sharp intensity decrease with increasing angle of incidence compared to the other SAM-treated NiO_x films (Figure S2), indicating that 4-NO_2-BA molecules are more parallel to the NiO_x surface than are the other SAMs.

Electrical and Optical Characterization. We performed Fourier transform infrared spectroscopy (FTIR) on NiO_x films treated with the SAMs and found that symmetric COO^- stretching vibrations appeared, indicating that the SAM molecules were bound to the NiO_x surface (Figure 2a). We carried out ultraviolet photoelectron spectroscopy (UPS) measurements of pristine NiO_x, SAM-treated NiO_x, and poly-TPD to determine work function (W_F) and the valence band maximum (VBM) (Figure S3). Pristine NiO_x showed a W_F of 5.0 eV and VBM of 5.4 eV. Three SAM-treated NiO_x films exhibited deeper W_F and VBM compared to pristine NiO_x (Figure 2b). Among these, 4-CF_3-BA-treated NiO_x films showed the highest W_F and VBM. Despite having a smaller intrinsic dipole compared to 4-NO_2-BA, the 4-CF_3-BA SAM induced the strongest total dipole on the NiO_x surface.

We further conducted scanning Kelvin probe microscopy (SKPM) to investigate two-dimensional distributions of contact potential differences (CPDs) of the SAM-treated NiO_x films. The SAM-treated NiO_x films showed higher CPDs compared to pristine NiO_x. The 4-CF_3-BA-treated NiO_x showed the highest CPDs (Figure 2c), consistent with the fact that it exhibited the largest W_F shift seen via UPS. In all instances, the variation of the CPD for different locations on the substrate showed a standard deviation of less than 15 mV, indicating a substantially spatially homogeneous W_F for SAM-treated NiO_x films.

To investigate the hole injection and transport properties of the different HILs, we fabricated hole-only devices with the structure ITO/NiO_x/SAMs/poly-TPD/InP@ZnSe@ZnS QDs/MoO_3/Ag, and we measured dark current (Figure 2d). SAM-treated devices showed 100-fold larger hole currents than those with pristine NiO_x, indicating improved hole injection.

To investigate the effect of SAMs on the optical properties of QDs, we measured time-resolved photoluminescence (PL)

https://doi.org/10.1021/jacs.2c09705
J. Am. Chem. Soc. XXXX, XXX, XXX−XXX

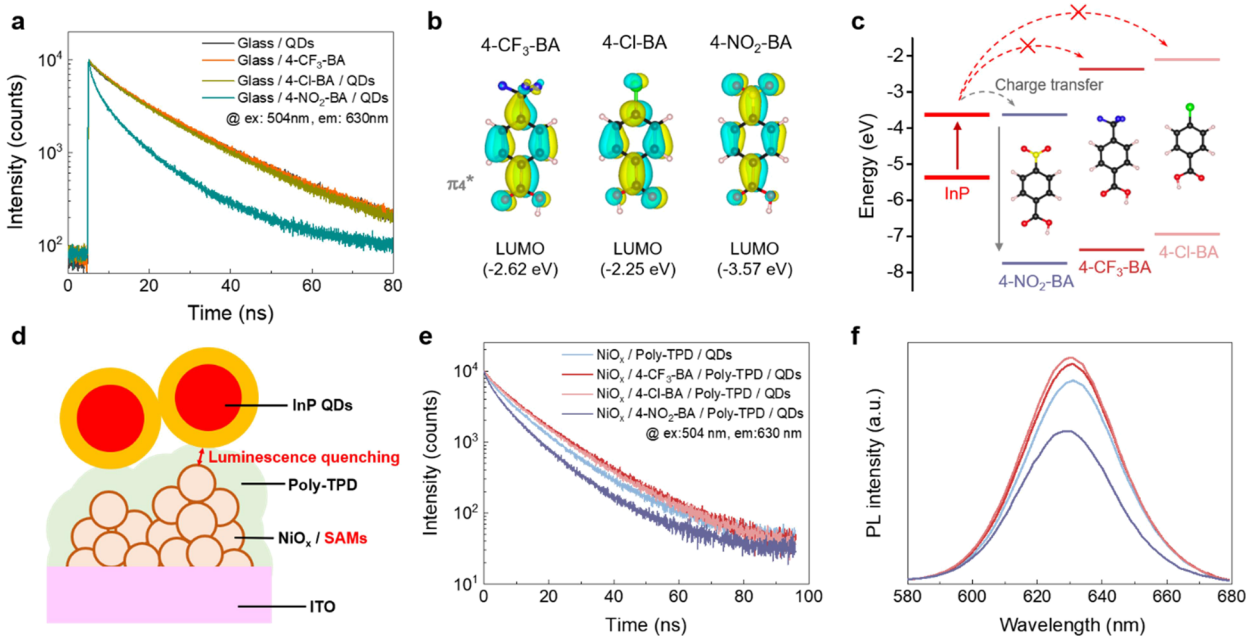

Figure 3. Luminescence quenching studies for QDs with SAMs. (a) Time-resolved PL spectra of QD solutions with the addition of SAMs. (b) Energy level and electron density distribution of LUMO for SAMs, calculated by HSE06. (c) Energy level schematic showing representing the luminescence quenching mechanism via electron transfer. (d) Schematic illustrations for the ITO/NiO_x/SAMs/poly-TPD/QD substrate. (e) Time-resolved PL spectra of ITO/NiO_x/SAMs/poly-TPD/QDs. (f) Steady-state PL spectra of ITO/NiO_x/SAMs/poly-TPD/QDs.

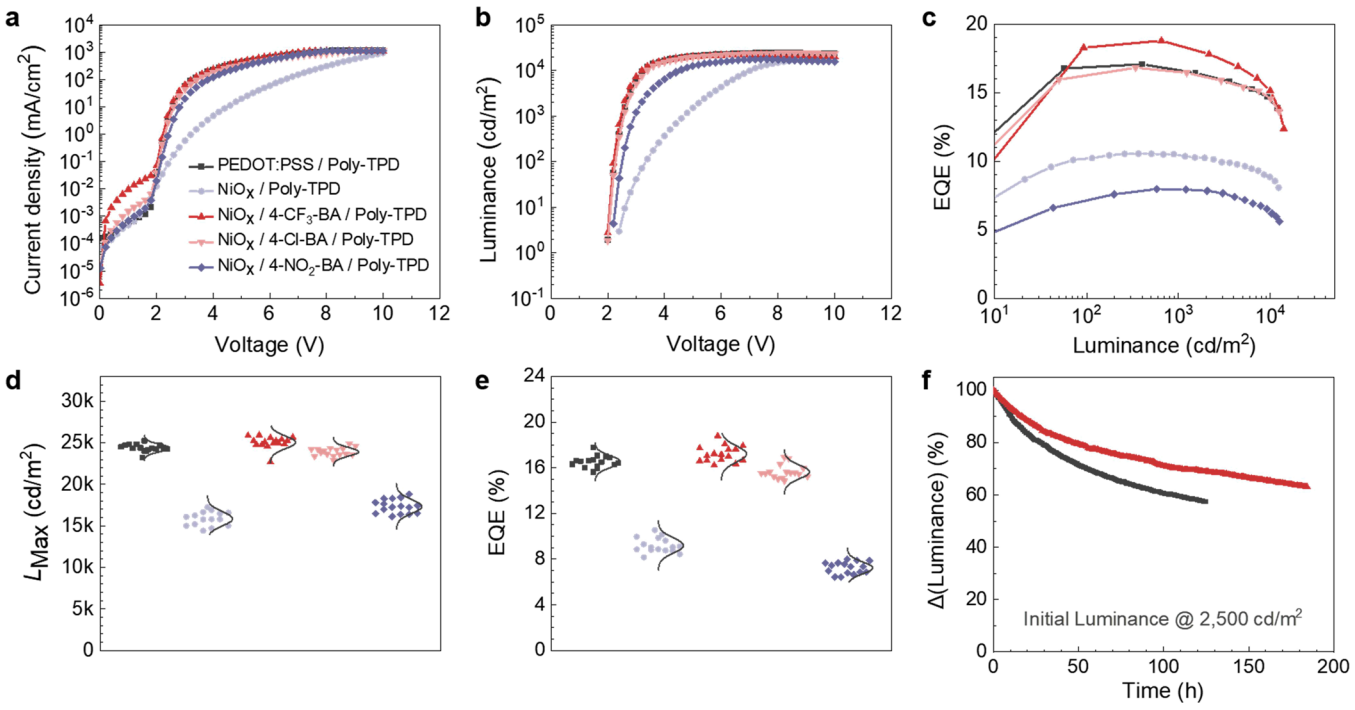

Figure 4. LED performance. (a) *J*–*V* characteristics of QLEDs with different HILs. (b) Luminance versus voltage characteristics of QLEDs with different HILs. (c) EQE versus voltage characteristics of QLEDs with different HILs. Statistics of (d) maximum luminance and (e) EQE from 16 devices with different HILs. (f) Operating stability of QLEDs with PEDOT:PSS and 4-CF_3-BA-treated NiO_x.

of the QD films deposited on SAM-coated glass substrates (Figure 3a). The QD films with 4-CF_3-BA and 4-Cl-BA showed PL decay dynamics similar to those of the pristine QD film. However, QD films with 4-NO_2-BA exhibited a substantially shorter PL lifetime, indicating fast exciton dissociation at the QD/SAM interface. In order to elucidate the effect of SAMs on the PL quenching of QDs, we carried out DFT calculations to determine the highest occupied molecular orbital (HOMO) and the LUMO levels of the SAMs (Figures 3b and S4). The strong electron-withdrawing NO_2 group—when attached to an aromatic ring—has the potential to delocalize π-electrons of the aromatic ring by resonance while at the same time compensating its own charge deficiency.[30,31] Delocalization of electrons increases molecular

https://doi.org/10.1021/jacs.2c09705
J. Am. Chem. Soc. XXXX, XXX, XXX−XXX

stability (the low potential energy), downshifting the HOMO and LUMO levels.[31,32] The DFT results indicate that 4-NO_2-BA has a deep LUMO level (−3.57 eV) that results in the electron transfer from QDs to the 4-NO_2-BA molecule (Figure 3c). This process causes the luminescence to quench, something observed in PL lifetime decay. We conclude that the 4-NO_2-BA SAM is not suitable for high-efficiency InP QLED applications.

We further characterized the optical properties of the QD films deposited on ITO/NiO_x/SAMs/poly-TPD substrates (Figure 3d−f) which are HIL/HTL combinations in QLEDs. We found that despite the presence of the organic poly-TPD layer on the HILs, the optical properties of the QD films still depend on the type of HILs (Figure S5). We used atomic force microscopy (AFM) to determine the coverage of the poly-TPD layer over the NiO_x film. We found that the pristine NiO_x exhibited a large height deviation of 23 nm between the maximum peak and the lowest valley (Figure S6). The poly-TPD film was optimized to be 25 nm and therefore is not thick enough to prevent charge or energy transfer between QDs and NiO_x. It is likely that the poly-TPD layer prevents direct contact between QDs and SAM-treated NiO_x, so that exchange between SAMs and native ligands of QDs is limited. We offer that QD-HIL photophysical interactions are chiefly responsible for the luminescence quenching rather than QD surface chemistry begin the prime factor. In locations where the peaks of NiO_x are observed, the QDs are in close proximity to the NiO_x-SAM stack, leading to nonradiative recombination on the NiO_x-SAM interface (Figure 3d). QD films on the layer stack containing 4-CF_3-BA and 4-Cl-BA SAMs showed a longer PL lifetime (11.1 and 10.7 ns) and higher PL intensity compared to the QD films on layer stacks without SAM (9.4 ns), which we attribute to the passivation of defects on NiO_x surfaces by the SAM. By contrast, the QD film with 4-NO_2-BA-treated NiO_x exhibited a reduced PL lifetime (7.0 ns) and PL intensity, indicative of luminescence quenching.

LED Performance. We fabricated QLEDs with device configuration ITO/PEDOT:PSS and ITO/SAM-treated NiO_x/Poly-TPD/QDs/ZnMgO/Al (Figure 4) and characterized them for current density, luminance, and EQE. QLEDs containing a SAM exhibit a current density at 3.0 V that is 100-fold higher compared to QLEDs without SAMs (Figure 4a), a finding we attribute to improved hole injection. They therefore exhibited a sharp increase in luminance with a lower turn-on voltage compared to QLEDs without SAMs (Figure 4b). Despite the improved current density for 4-NO_2-BA-containing QLEDs, they showed a lower EQE (8.0%) than those without SAM addition (10.5%) because of luminescence quenching caused by the SAM (Figure 4c). In contrast, QLEDs containing 4-CF_3-BA and 4-Cl-BA exhibited improved luminance and EQE compared to QLEDs without SAMs (Figure 4b,c), a finding we attribute to improved hole injection and suppressed luminescence quenching. Champion devices contained the 4-CF_3-BA SAM, and yielded LED performance exhibiting a maximum luminance of 22,300 cd m^{-2}, EQE of 18.8%, and turn-on voltage of 2.0 V. Based on total 80 devices, the average maximum luminance and EQE values (25,000 cd m^{-2} and 17.2%) of QLEDs with 4-CF_3-BA-treated NiO_x are statistically higher than those (24,500 cd m^{-2} and 16.1%) of the devices made with the PEDOT:PSS HIL (Figure 4d,e).

Balanced charge injection/transport into the light-emitting QD layer is also indicated by capacitance versus voltage ($C-V$) characterization (Figure S7). The capacitance of QLEDs increased near the turn-on voltage, something we assign to the injection and accumulation of electrons, and it then decreased due to the recombination of injected holes with accumulated electrons in the QD layer. 4-CF_3-BA-treated QLEDs exhibited the lowest onset voltage for the drop-in capacitance, indicating the most efficient charge recombination facilitated by the improved hole injection/transport. We evaluated further the impact of SAMs on the performance of QLEDs by simulating the hole concentration in the QD layer (Figure S8). The device model replicates the role of the dipole moment at the NiO_x surface in facilitating hole injection and increasing hole density in the QD layer to improve EQE (Figure S8).

We then investigated the operating stability of encapsulated devices under ambient conditions, applying a constant current density around 20 mA cm^{-2} (Figure 4f), corresponding to an initial luminance of 2500 cd m^{-2}. We monitored the evolution of luminance as a function of operating time and found that the QLEDs with 4-CF_3-BA NiO_x exhibited improved operating stability compared to the QLEDs with PEDOT:PSS, retaining 75% of initial luminance following 74 h (T_{75}).

CONCLUSIONS

In summary, we explored the replacement of a PEDOT:PSS HIL with inorganic NiO_x toward the goal of addressing instability in QLEDs, an instability linked with PEDOT:PSS acidic and hygroscopic nature. We found that pristine NiO_x has an unfavorable band alignment with InP/ZnSe/ZnS QD and induces a luminescence quenching of QDs. We employed SAMs based on BA derivatives and found that molecular orientation is a critical parameter for tuning the energy levels of NiO_x. We found that the strongest intrinsic dipole was realized with 4-NO_2-BA. In contrast, 4-CF_3-BA-treated NiO_x exhibited deeper energy levels than 4-NO_2-BA-treated NiO_x, which we found to originate from the more perpendicular orientation of 4-CF_3-BA compared to 4-NO_2-BA on the NiO_x surface. We found that the NO_2 group delocalizes electrons of the aromatic ring, downshifting its LUMO level to a level close to that of the conduction band of the InP core. This band alignment resulted in luminescence quenching via electron transfer from QDs to the 4-NO_2-BA molecules. The 4-CF_3-BA SAM provided the optimal amount of shift in energy levels and also achieved passivation of surface defect states of NiO_x. The best interface molecules enabled NiO_x HILs with efficient hole injection and reduced quenching of luminescence. As a result, we demonstrated efficient QLEDs achieving EQE 18.8%, a record, to our knowledge, among inorganic HIL-based QLEDs.

EXPERIMENTAL SECTION

Materials. NiO_x nanoparticles (Avantama, P-21, 0.15 wt %), BA (99.5%, Sigma-Aldrich), 4-Cl-BA (99%, Sigma-Aldrich), 4-CF_3-BA (98%, Sigma-Aldrich), 4-NO_2-BA (98%, Sigma-Aldrich), PEDOT:PSS (Ossila, M121, AI4083), and poly-TPD (American Dye Sources Inc., ADS254BE) were used without further purification.

QD Synthesis. The red-emitting InP/ZnSe/ZnS QDs were prepared according to a previously reported method.[10] For the synthesis of the InP core, 4 mmol of indium palmitate was prepared in 100 mL of 1-octadecene by degassing at 120 °C for 1 h. Then, the solution was heated to 280 °C under N_2 condition and 2 mmol of 0.2 M tris(trimethylsilyl)phosphine/trioctylphosphine (TOP) was quickly injected to the solution. The reaction temperature was kept at 260 °C. For further growth of the InP cores, 10.5 mmol of 0.2 M indium palmitate and 5.26 mmol of 0.2 M tris(trimethylsilyl)-phosphine were added into the flask for 35 min at 260 °C. The InP core was purified and dispersed in toluene for the shell growth. 1.6

https://doi.org/10.1021/jacs.2c09705
J. Am. Chem. Soc. XXXX, XXX, XXX−XXX

mmol of zinc oleate was prepared in 80 mL of trioctylamine by degassing at 120 °C for 1 h. Then, the solution was heated to 180 °C under N_2 flow, and 0.25 g of InP core and 0.2 mL of hydrofluoric acid solution (10 wt %) were added into the solution. The reaction temperature was kept at 340 °C. 17.6 mmol of 0.4 M zinc oleate and 16 mmol of 0.4 M Se/TOP were added into the solution for ZnSe shell growth. Then, 4.8 mmol of 0.4 M zinc oleate and 6.4 mmol of 1 M S/TOP were added for ZnS shell growth. The synthesized red-emitting InP/ZnSe/ZnS QDs showed the emission band at 630 nm, a full width at half-maximum of 35 nm, and quantum yield over 90%. The QDs were purified with ethanol and dispersed in octane for LED fabrication.

Device Fabrication. The prepatterned ITO glasses were sequentially sonicated in deionized water, acetone, and 2-propanol each for 5 min. After drying with nitrogen, the substrates were exposed to UV-ozone treatment for 15 min to remove organic contaminants. PEDOT:PSS (Ossila, M121, AI4083) solution was spun-cast on the substrates at 4000 rpm for 30 s after filtering through a 0.45 μm polyvinylidene fluoride membrane, and then PEDOT:PSS films were annealed at 130 °C for 10 min. For NiO_x films, 150 μL of diluted NiO_x nanoparticle dispersions (Avantama, P-21, 0.15 wt %) was filtered through a 0.22 μm polytetrafluoroethylene (PTFE) membrane before use and spun-cast at 3000 rpm for 30 s and annealed at 100 °C for 10 min. Annealed NiO_x films were UV-ozone treated for 3 min. NiO_x substrates were soaked with SAM solutions (2.5 mg/mL in anhydrous ethanol) for 30 s, and spin-cast at 5000 rpm for 20 s, and then annealed at 100 °C for 5 min. Unbound SAM molecules were washed off with pure anhydrous ethanol spin coating at 5000 rpm for 20 s and annealed at 100 °C for 5 min. All HIL coated substrates was transferred in the N_2-filled glovebox, and then 150 μL of poly-TPD (American Dye Sources Inc., ADS254BE) in chlorobenzene (6 mg/mL) solution was filtered through a 0.22 μm PTFE membrane before use and spun-cast at 3000 rpm for 30 s. The films were annealed at 150 °C for 15 min. InP QD solution was filtered through a 0.22 μm PTFE membrane before use and spun-cast at 3000 rpm for 30 s followed by annealing at 150 °C for 15 min. After cooling down, ZnMgO nanoparticle dispersions in anhydrous ethanol (70 mg/mL) was filtered through a 0.22 μm PTFE membrane before use and spun-cast at 3000 rpm for 30 s followed by annealing at 150 °C for 15 min. The films were then transferred to the thermal evaporator (Angstrom engineering), and a patterned Al electrode (100 nm thick) was deposited on top of ZnMgO with a rate of 1.0 Å/s under a vacuum pressure less than 2×10^{-6} Torr.

NEXAFS Spectra at Various Incident Angles. NEXAFS spectra of SAMs on NiO_x were measured at various incident angles from 20 to 90° in total X-ray electron yield mode at room temperature using BL-20A at NSRRC. The samples were subjected to an ultrahigh vacuum chamber (1×10^{-9} Torr). The area under spectra was fixed over an energy range of 270−300 eV for C K-edge.

LED Performance and Stability Measurement. The $J-V$ characteristics of LEDs were recorded using a Keithley 647 source meter. Electroluminescence spectra and luminance at a certain $J-V$ point were measured using a calibrated fiber-coupled spectrometer (QE-pro, Ocean Optics) and an integrating sphere.

Hole-Only Device Fabrication and Measurement. Hole-only devices with the structure of Glass/ITO/HIL/poly-TPD/InP QD/MoO_x/Ag were fabricated. PEDOT:PSS, NiO_x, SAMs, poly-TPD, InP QD, and Ag were fabricated under the same conditions for device fabrication. 10 nm thick MoO_x was deposited with a rate of 0.1 Å/s under a vacuum pressure less than 2×10^{-6} Torr. The $J-V$ characteristics of hole-only device were measured with a Keithley 2400 source measuring unit.

Steady-State and Time-Resolved PL Measurement. Steady-state PL and time-resolved PL were measured using a Horiba Fluorolog system. A monochromatized xenon lamp was used as the excitation source for steady-state PL. A pulsed laser diode and a time-correlated single-photon counting detector were used for time-resolved PL. The excitation wavelength was 510 nm for both steady-state PL and time-resolved PL measurement.

DFT Calculation. The whole DFT calculations in this work are done by FHI-aims code[33−35] The default numerical settings, referred to as "tight" in FHI-aims were used. Spin-polarized treatment for Ni atom was incorporated into all calculated electronic properties and geometry relaxations. More specifically, the NiO_x in all structures (i.e., unit cell, slabs) adopt a type-II antiferromagnetic phase (i.e., the spin ordering vector is along the [111] direction), as shown in Figure S1a. Local minimum-energy geometries of the Born−Oppenheimer surface were obtained with residual total energy gradients below 1×10^{-2} eV/Å for atomic positions by Perdew-Burke-Ernzerhof-generalized gradient approximation functional[36,37] within the Van der Waals corrections followed by the Tkatchenko−Scheffler method.[38] More details can be found in the Supporting Information.

SKPM. SKPM was conducted using a Ti/Ir coated AFM tip (ASYELEC.01-R2, f = 79.029 kHz, k = 3.79 N/m) on an MFP-3D AFM (Asylum Research). The tip's deflection sensitivity and stiffness were calibrated using Sader's method.[39,40] A two-path scanning mode was adopted where the first path scans the topography of the sample, and the second path measures the CPD between the tip and the sample. In the second path, the tip was raised 20 nm above the surface and applied 1 V of electrical driving amplitude. The images were collected at a scan rate of 0.5 Hz.

Other Characterization. FTIR spectra were obtained using a Thermo Scientific iS50 Spectral range 4600−50 cm^{-1} with ATR accessory. Samples were prepared on a glass substrates. AFM measurement was done using an Asylum Research Cipher AFM. UPS measurement was performed at nanoFAB, University of Alberta, using a Kratos Axis Ultra spectrometer. UPS was performed with a He I source ($h\nu$ = 21.2 eV). The sample was measured under −10 V bias. The power for UPS was 3 kV × 20 mA (60 W).

■ ASSOCIATED CONTENT

Supporting Information

The Supporting Information is available free of charge at https://pubs.acs.org/doi/10.1021/jacs.2c09705.

Type II antiferromagnetic phase of NiO_x, atomic ratio of SAM-treated NiO_x films from XPS analysis, details on DFT calculations, NEXAFS, UPS, HODs, and AFM, energy level and electron density distribution, time-resolved PL spectra of QD films, ($C-V$) characteristics of QLEDs, and simulation of LEDs (PDF)

■ AUTHOR INFORMATION

Corresponding Author

Edward H. Sargent − *Department of Electrical and Computer Engineering, University of Toronto, Toronto, Ontario M5S 1A4, Canada;* orcid.org/0000-0003-0396-6495; Email: ted.sargent@utoronto.ca

Authors

Seungjin Lee − *Department of Electrical and Computer Engineering, University of Toronto, Toronto, Ontario M5S 1A4, Canada;* Present Address: Department of Energy Engineering, KI for Energy Materials and Devices, Korea Institute of Energy Technology (KENTECH), Kentech-gil 21, Naju-si, Jeollanam-do 58330, Republic of Korea (S.L.); orcid.org/0000-0002-6318-0702

So Min Park − *Department of Electrical and Computer Engineering, University of Toronto, Toronto, Ontario M5S 1A4, Canada*

Eui Dae Jung − *Department of Electrical and Computer Engineering, University of Toronto, Toronto, Ontario M5S 1A4, Canada; Department of Applied Chemistry, National Yang Ming Chiao Tung University, Hsinchu 300, Taiwan*

https://doi.org/10.1021/jacs.2c09705
J. Am. Chem. Soc. XXXX, XXX, XXX−XXX

Tong Zhu − *Department of Electrical and Computer Engineering, University of Toronto, Toronto, Ontario M5S 1A4, Canada; Department of Applied Chemistry, National Yang Ming Chiao Tung University, Hsinchu 300, Taiwan*
Joao M. Pina − *Department of Electrical and Computer Engineering, University of Toronto, Toronto, Ontario M5S 1A4, Canada;* orcid.org/0000-0002-3448-0028
Husna Anwar − *Department of Electrical and Computer Engineering, University of Toronto, Toronto, Ontario M5S 1A4, Canada*
Feng-Yi Wu − *Department of Applied Chemistry, National Yang Ming Chiao Tung University, Hsinchu 300, Taiwan*
Guan-Lin Chen − *Department of Applied Chemistry, National Yang Ming Chiao Tung University, Hsinchu 300, Taiwan*
Yitong Dong − *Department of Electrical and Computer Engineering, University of Toronto, Toronto, Ontario M5S 1A4, Canada*
Teng Cui − *Department of Mechanical and Industrial Engineering, University of Toronto, Toronto, Ontario M5S 3G8, Canada;* orcid.org/0000-0002-3218-2721
Mingyang Wei − *Department of Electrical and Computer Engineering, University of Toronto, Toronto, Ontario M5S 1A4, Canada*
Koen Bertens − *Department of Electrical and Computer Engineering, University of Toronto, Toronto, Ontario M5S 1A4, Canada;* orcid.org/0000-0002-2701-1397
Ya-Kun Wang − *Department of Electrical and Computer Engineering, University of Toronto, Toronto, Ontario M5S 1A4, Canada*
Bin Chen − *Department of Electrical and Computer Engineering, University of Toronto, Toronto, Ontario M5S 1A4, Canada;* orcid.org/0000-0002-2106-7664
Tobin Filleter − *Department of Mechanical and Industrial Engineering, University of Toronto, Toronto, Ontario M5S 3G8, Canada;* orcid.org/0000-0003-2609-4773
Sung-Fu Hung − *Department of Electrical and Computer Engineering, University of Toronto, Toronto, Ontario M5S 1A4, Canada; Department of Applied Chemistry, National Yang Ming Chiao Tung University, Hsinchu 300, Taiwan*
Yu-Ho Won − *Samsung Advanced Institute of Technology, Samsung Electronics, Suwon-si 16678, Republic of Korea;* orcid.org/0000-0002-6065-7800
Kwang Hee Kim − *Samsung Advanced Institute of Technology, Samsung Electronics, Suwon-si 16678, Republic of Korea*
Sjoerd Hoogland − *Department of Electrical and Computer Engineering, University of Toronto, Toronto, Ontario M5S 1A4, Canada;* orcid.org/0000-0002-3099-585X

Complete contact information is available at: https://pubs.acs.org/10.1021/jacs.2c09705

Author Contributions

#S.L., S.M.P., E.D.J., and T.Z. contributed equally to this work.

Notes

The authors declare no competing financial interest.

■ ACKNOWLEDGMENTS

This work was supported by Samsung Electronics Co. (MRA 211815). S.-F.H. thanks the support from the Ministry of Science and Technology, Taiwan (Contract No. MOST 111-2628-M-A49-007), and from the Yushan Young Scholar Program, Ministry of Education, Taiwan. T.F. and T.C. acknowledge financial support from the Canadian Foundation for Innovation (CFI) and the Natural Science and Engineering Council of Canada (NSERC). S.L. acknowledges financial support from the KENTECH Research Grant (202200012A) and a National Research Foundation of Korea (NRF) grant funded by the Government of Korea (MIST) (2022R1C1C1010034). We thank D. Kopilovic, E. Palmiano, L. Levina, and R. Wolowiec for the technical support.

■ REFERENCES

(1) Han, M. G.; Lee, Y.; Kwon, H.-I.; Lee, H.; Kim, T.; Won, Y.-H.; Jang, E. InP-Based Quantum Dot Light-Emitting Diode with a Blended Emissive Layer. *ACS Energy Lett.* **2021**, *6*, 1577−1585.
(2) Colvin, V. L.; Schlamp, M. C.; Alivisatos, A. P. Light-emitting diodes made from cadmium selenide nanocrystals and a semiconducting polymer. *Nature* **1994**, *370*, 354−357.
(3) Shirasaki, Y.; Supran, G. J.; Bawendi, M. G.; Bulović, V. Emergence of colloidal quantum-dot light-emitting technologies. *Nat. Photon.* **2013**, *7*, 13−23.
(4) Dai, X.; Zhang, Z.; Jin, Y.; Niu, Y.; Cao, H.; Liang, X.; Chen, L.; Wang, J.; Peng, X. Solution-processed, high-performance light-emitting diodes based on quantum dots. *Nature* **2014**, *515*, 96−99.
(5) Shen, H.; Gao, Q.; Zhang, Y.; Lin, Y.; Lin, Q.; Li, Z.; Chen, L.; Zeng, Z.; Li, X.; Jia, Y.; Wang, S.; du, Z.; Li, L. S.; Zhang, Z. Visible quantum dot light-emitting diodes with simultaneous high brightness and efficiency. *Nat. Photon.* **2019**, *13*, 192−197.
(6) Xiang, C.; Wu, L.; Lu, Z.; Li, M.; Wen, Y.; Yang, Y.; Liu, W.; Zhang, T.; Cao, W.; Tsang, S.-W.; et al. High efficiency and stability of ink-jet printed quantum dot light emitting diodes. *Nat. Commun.* **2020**, *11*, 1646.
(7) Cao, W.; Xiang, C.; Yang, Y.; Chen, Q.; Chen, L.; Yan, X.; Qian, L. Highly stable QLEDs with improved hole injection via quantum dot structure tailoring. *Nat. Commun.* **2018**, *9*, 2608.
(8) Lee, T.; Kim, B. J.; Lee, H.; Hahm, D.; Bae, W. K.; Lim, J.; Kwak, J. Bright and Stable Quantum Dot Light-Emitting Diodes. *Adv. Mater.* **2022**, *34*, No. 2106276.
(9) Li, Y.; Hou, X.; Dai, X.; Yao, Z.; Lv, L.; Jin, Y.; Peng, X. Stoichiometry-Controlled InP-Based Quantum Dots: Synthesis, Photoluminescence, and Electroluminescence. *J. Am. Chem. Soc.* **2019**, *141*, 6448−6452.
(10) Won, Y.-H.; Cho, O.; Kim, T.; Chung, D.-Y.; Kim, T.; Chung, H.; Jang, H.; Lee, J.; Kim, D.; Jang, E. Highly efficient and stable InP/ZnSe/ZnS quantum dot light-emitting diodes. *Nature* **2019**, *575*, 634−638.
(11) Gao, M.; Yang, H.; Shen, H.; Zeng, Z.; Fan, F.; Tang, B.; Min, J.; Zhang, Y.; Hua, Q.; Li, L. S.; et al. Bulk-like ZnSe Quantum Dots Enabling Efficient Ultranarrow Blue Light-Emitting Diodes. *Nano Lett.* **2021**, *21*, 7252−7260.
(12) Meng, Y.; Hu, Z.; Ai, N.; Jiang, Z.; Wang, J.; Peng, J.; Cao, Y. Improving the Stability of Bulk Heterojunction Solar Cells by Incorporating pH-Neutral PEDOT:PSS as the Hole Transport Layer. *ACS Appl. Mater. Interfaces* **2014**, *6*, 5122−5129.
(13) Yun, J.-M.; Yeo, J.-S.; Kim, J.; Jeong, H.-G.; Kim, D.-Y.; Noh, Y.-J.; Kim, S.-S.; Ku, B.-C.; Na, S.-I. Solution-Processable Reduced Graphene Oxide as a Novel Alternative to PEDOT:PSS Hole Transport Layers for Highly Efficient and Stable Polymer Solar Cells. *Adv. Mater.* **2011**, *23*, 4923−4928.
(14) Choi, H.; Mai, C.-K.; Kim, H.-B.; Jeong, J.; Song, S.; Bazan, G. C.; Kim, J. Y.; Heeger, A. J. Conjugated polyelectrolyte hole transport layer for inverted-type perovskite solar cells. *Nat. Commun.* **2015**, *6*, 7348.
(15) Cameron, J.; Skabara, P. J. The damaging effects of the acidity in PEDOT:PSS on semiconductor device performance and solutions based on non-acidic alternatives. *Mater. Horiz.* **2020**, *7*, 1759−1772.
(16) Lin, J.; Dai, X.; Liang, X.; Chen, D.; Zheng, X.; Li, Y.; Deng, Y.; Du, H.; Ye, Y.; Chen, D.; Lin, C.; Ma, L.; Bao, Q.; Zhang, H.; Wang, L.; Peng, X.; Jin, Y. High-Performance Quantum-Dot Light-Emitting

Diodes Using NiO_x Hole-Injection Layers with a High and Stable Work Function. *Adv. Funct. Mater.* **2020**, *30*, No. 1907265.
(17) Chen, W.-S.; Yang, S.-H.; Tseng, W.-C.; Chen, W. W.-S.; Lu, Y.-C. Utilization of Nanoporous Nickel Oxide as the Hole Injection Layer for Quantum Dot Light-Emitting Diodes. *ACS Omega* **2021**, *6*, 13447−13455.
(18) Caruge, J.-M.; Halpert, J. E.; Bulović, V.; Bawendi, M. G. NiO as an Inorganic Hole-Transporting Layer in Quantum-Dot Light-Emitting Devices. *Nano Lett.* **2006**, *6*, 2991−2994.
(19) Singh, N.; Tao, Y.-T. Effect of surface modification of nickel oxide hole-transport layer via self-assembled monolayers in perovskite solar cells. *Nano Sel.* **2021**, *2*, 2390−2399.
(20) Wang, L.; Pan, J.; Qian, J.; Liu, C.; Zhang, W.; Akram, J.; Lei, W.; Chen, J. Performance Enhancement of All-Inorganic Quantum Dot Light-Emitting Diodes via Surface Modification of Nickel Oxide Nanoparticles Hole Transport Layer. *ACS Appl. Electron. Mater.* **2019**, *1*, 2096−2102.
(21) Al-Ashouri, A.; Magomedov, A.; Roß, M.; Jošt, M.; Talaikis, M.; Chistiakova, G.; Bertram, T.; Márquez, J. A.; Köhnen, E.; Kasparavičius, E.; et al. Conformal monolayer contacts with lossless interfaces for perovskite single junction and monolithic tandem solar cells. *Energy Environ. Sci.* **2019**, *12*, 3356−3369.
(22) Wang, Q.; Chueh, C.-C.; Zhao, T.; Cheng, J.; Eslamian, M.; Choy, W. C. H.; Jen, A. K. Y. Effects of Self-Assembled Monolayer Modification of Nickel Oxide Nanoparticles Layer on the Performance and Application of Inverted Perovskite Solar Cells. *ChemSusChem* **2017**, *10*, 3794−3803.
(23) Singh, N.; Mohapatra, A.; Chu, C.-W.; Tao, Y.-T. Modulation of work function of ITO by self-assembled monolayer and its effect on device characteristics of inverted perovskite solar cells. *Org. Electron.* **2021**, *98*, No. 106297.
(24) Heyd, J.; Scuseria, G. E.; Ernzerhof, M. Hybrid functionals based on a screened Coulomb potential. *J. Chem. Phys.* **2003**, *118*, 8207−8215.
(25) Heyd, J.; Scuseria, G. E.; Ernzerhof, M. Erratum: "Hybrid functionals based on a screened Coulomb potential" [J. Chem. Phys. 118, 8207 (2003)]. *J. Chem. Phys.* **2006**, *124*, 219906.
(26) Chen, W.; Wee, A. T. S. Synchrotron PES and NEXAFS studies of self-assembled aromatic thiol monolayers on Au(111). *J. Electron Spectrosc. Relat. Phenom.* **2009**, *172*, 54−63.
(27) Baio, J. E.; Jaye, C.; Fischer, D. A.; Weidner, T. High-Throughput Analysis of Molecular Orientation on Surfaces by NEXAFS Imaging of Curved Sample Arrays. *ACS Comb. Sci.* **2014**, *16*, 449−453.
(28) Peisert, H.; Schwieger, T.; Auerhammer, J. M.; Knupfer, M.; Golden, M. S.; Fink, J.; Bressler, P. R.; Mast, M. Order on disorder: Copper phthalocyanine thin films on technical substrates. *J. Appl. Phys.* **2001**, *90*, 466−469.
(29) Chen, W.; Wang, L.; Qi, D. C.; Chen, S.; Gao, X. Y.; Wee, A. T. S. Probing the ultrafast electron transfer at the CuPc/Au(111) interface. *Appl. Phys. Lett.* **2006**, *88*, 184102.
(30) Ju, K.-S.; Parales, R. E. Nitroaromatic Compounds, from Synthesis to Biodegradation. *Microbiol. Mol. Biol. Rev.* **2010**, *74*, 250−272.
(31) Farley, C.; Aggarwal, A.; Singh, S.; Dolor, A.; Falber, A.; Crossley, M.; Drain, C. M. A Structural Model of Nitro-Porphyrin Dyes Based on Spectroscopy and Density Functional Theory. *J. Comput. Chem.* **2018**, *39*, 1129−1142.
(32) Yang, H.; Cui, C.; Li, Y. Effects of Heteroatom Substitution on the Photovoltaic Performance of Donor Materials in Organic Solar Cells. *Acc. Mater. Res.* **2021**, *2*, 986−997.
(33) Blum, V.; Gehrke, R.; Hanke, F.; Havu, P.; Havu, V.; Ren, X.; Reuter, K.; Scheffler, M. Ab initio molecular simulations with numeric atom-centered orbitals. *Comput. Phys. Commun.* **2009**, *180*, 2175−2196.
(34) Havu, V.; Blum, V.; Havu, P.; Scheffler, M. Efficient O(N) integration for all-electron electronic structure calculation using numeric basis functions. *J. Comput. Phys.* **2009**, *228*, 8367−8379.
(35) Ruschhaupt, A.; Chen, X.; Alonso, D.; Muga, J. G. Optimally robust shortcuts to population inversion in two-level quantum systems. *New J. Phys.* **2012**, *14*, No. 093040.
(36) Hunsche, S.; Starczewski, T.; l'Huillier, A.; Persson, A.; Wahlström, C. G.; van Linden van den Heuvell, H. B.; Svanberg, S. Ionization and Fragmentation of C60 via Multiphoton-Multiplasmon Excitation. *Phys. Rev. Lett.* **1996**, *77*, 1966−1969.
(37) Perdew, J. P.; Burke, K.; Ernzerhof, M. Generalized Gradient Approximation Made Simple. *Phys. Rev. Lett.* **1996**, *77*, 3865−3868.
(38) Tkatchenko, A.; Scheffler, M. Accurate Molecular Van Der Waals Interactions from Ground-State Electron Density and Free-Atom Reference Data. *Phys. Rev. Lett.* **2009**, *102*, No. 073005.
(39) Sader, J. E.; Sanelli, J. A.; Adamson, B. D.; Monty, J. P.; Wei, X.; Crawford, S. A.; Friend, J. R.; Marusic, I.; Mulvaney, P.; Bieske, E. J. Spring constant calibration of atomic force microscope cantilevers of arbitrary shape. *Rev. Sci. Instrum.* **2012**, *83*, 103705.
(40) Sader, J. E.; Lu, J.; Mulvaney, P. Effect of cantilever geometry on the optical lever sensitivities and thermal noise method of the atomic force microscope. *Rev. Sci. Instrum.* **2014**, *85*, 113702.

https://doi.org/10.1021/jacs.2c09705
J. Am. Chem. Soc. XXXX, XXX, XXX−XXX